

Bond breaking of furan-maleimide adducts via a diradical sequential mechanism under an external mechanical force

Manuel Cardosa-Gutierrez,¹ Guillaume De Bo,² Anne-Sophie Duwez,¹ *Francoise Remacle¹

¹ UR Molecular Systems, Department of Chemistry, University of Liège, 4000 Liège, Belgium

² Department of Chemistry, University of Manchester, Manchester M13 9PL, UK

Electronic Supplementary Information

Computational details

S1 Comparison between the UDFT and the CAS(4,4) CoGEF paths.

S2 Choice of the functional for the UDFT computation.

S3 Activation barriers and rate constants for the breaking of the first scissile bonds.

S4 Diradical character of S_0 and T_0 and spin-orbit interaction.

ZIP files

S5 Geometries along the CoGEF path for the P_{endo} and P_{exo} adducts computed at the DFT/wB97XD/6-31G(d,p) level.

S6 Geometries along the CoGEF path for the P_{endo} and P_{exo} adducts computed at the CAS(4,4)/6-31G(d,p) level for S_0 .

S7 Geometries of the reactant and transition states computed as a function of the external force at the wB97XD/6-31G(d,p) level.

S8 Geometries at the S_0/T_0 MEIC for the P_{endo} and P_{exo} adducts computed at the CAS(4,4)/6-31G(d,p) level.

S1. Comparison between the UDFT and the CAS(4,4) CoGEF paths

The reaction mechanism was studied by the CoGEF isometric protocol¹ for the two adducts at the UDFT level with the wB97XD² and at the complete active space³ CAS-SCF (4,4) level with the 6-31G(d,p) basis set for the lowest singlet, S₀. Files of the geometries along the CoGEF path computed at the DFT and the CAS(4,4) level are given in the SI (S5 and S6).

The computed force modified minimum energy paths are fully consistent, as can be seen from Figure S1, as well as the relaxed geometries obtained for each value of the applied distortion.

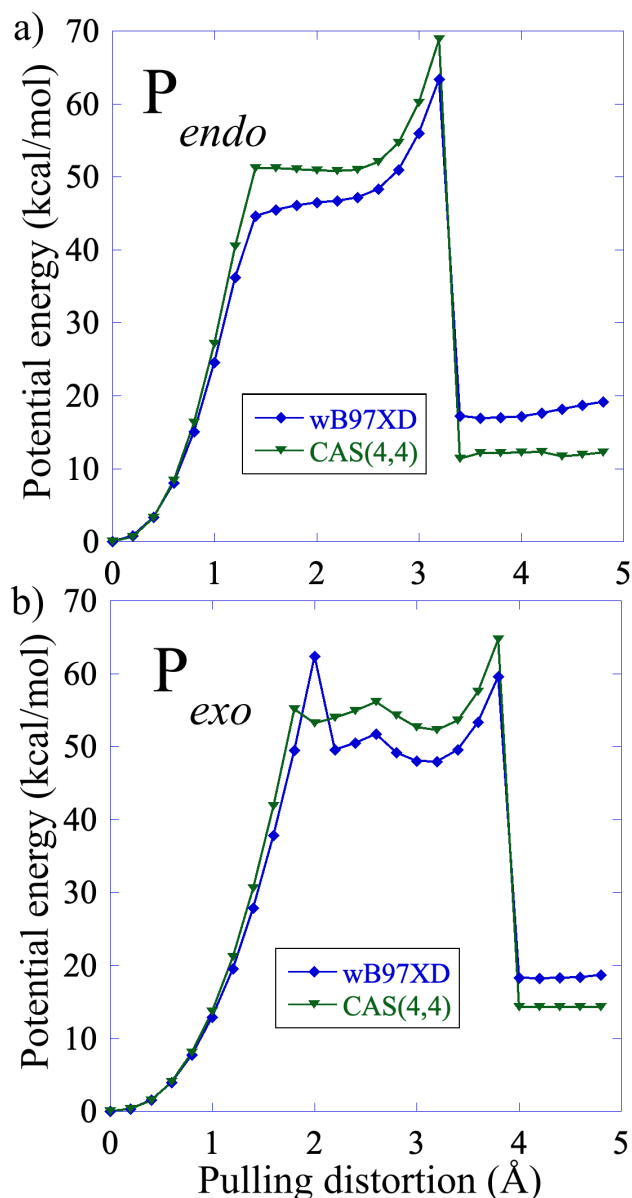


Figure S1 Comparison between the CAS (4,4) CoGEF path and the UDFT/wB97XD with 6-31G(d,p) for the P_{endo} and P_{exo} adducts.

S2 Choice of the functional for the UDFT computation

In order to properly describe the diradical character of the open shell S_0 state in the intermediate region, we use the range-separated hybrid functional wB97XD.² PBE0DH⁴ and BH&HLYP⁵ which includes 50% not Coulomb-attenuated HF exchange gives similar results. A D3 Grimme correction^{2,6} was used for the BH&HLYP and PBE0DH computations.

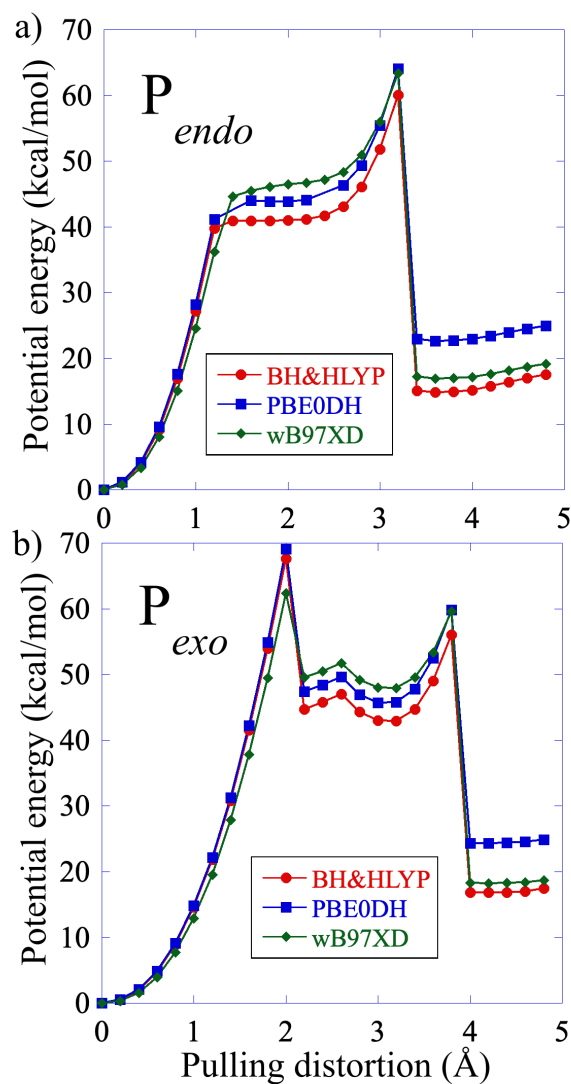


Figure S2 Energy profiles and activation barriers for the P_{endo} (a) and the P_{exo} (b) adducts computed with the WB97XD, BH&HLYP and PBE0DH functionals.

The UDFT computations were carried out with the quantum chemistry software QChem v5.4⁷ and the CAS-SCF computation with the quantum chemistry code MOLPRO 2021.^{8,9}

S3 Activation barriers and rate constants for the breaking of the first scissile bond

The activation free energy ($\Delta^\ddagger G^0$) for the four adducts was computed at room temperature, for different values of the force by taking the difference between the free energy of the transition states (TS) and the equilibrium geometries (Eq. 1). A vibrational analysis of the optimized TS and equilibrium geometries was carried out for each adduct under force using the EFEI approach in order to compute the free energy.

$$\Delta G^{\ddagger 0} = G^0(TS) - G^0(Eq) \quad (S1)$$

The rates constants at a given temperature ($k(T)$) are estimated using Eyring transition states theory:

$$k(T) = \frac{k_B T}{h c^0} e^{-\Delta G^{\ddagger 0}/RT} \quad (S2)$$

- $c^0 = 1$ is the standard concentration.
- $\Delta G^{\ddagger 0}$ is the free energy of activation, and T is the temperature.
- $k_B, h, R,$ are Boltzmann, Planck, and ideal gas constants, respectively.

At zero force, at 298 K, at the DFT wb97XD/6-31G(p,d) level that we use, we compute values of 28.2 kcal/mol and 30.8 kcal/mol for the barrier of the concerted rupture of the P_{endo} and P_{exo} adducts in the gas phase, which leads to a $\Delta(\Delta G^\ddagger)$ value of 2.6 kcal/mol. These values are higher than the values reported by Craig et al in ref¹⁰. Craig et al report 22.8 and 24.8 kcal/mol respectively for computations at the B3LYP/6-31G(d) level in THF for a slightly longer acetoxy anchoring chains (CH₂-O-CO-CH₃ on furane and CH₂-CH₂-O-CO-CH₃ on maleimide instead of CH₃ in our computations). Their $\Delta(\Delta G^\ddagger)$ of 2.2 kcal/mol between the P_{endo} and P_{exo} adducts is in good agreement with our computed values. Our computed values are closer to those reported by Meir et al in the gas phase (ref¹¹) (30.9 and 32.3 kcal/mol) at the B3LYP/6-311++G(d,p) for geometry optimization carried out at the BP86/6-31G(d) level. They are \approx 2-3 kcal higher than those of Yang et al (ref¹²): 25.1 and 28.9 kcal/mol computed at the M06-2X/6-311+G(d,p) level in DMSO using a SMD solvation model and those of Rulisek et al¹³ (24.6 kcal/mol and 26.4 kcal/mol) obtained in the gas phase from equilibrium geometries at the MP2/6-31G(d) level and a single point CCSD(T) computation with a Aug-cc-pVDZ basis set.

A full geometry optimization at the BH&HLYP/6-31G(d,p) level gives barriers of 30.51 kcal/mol and 32.24 kcal/mol for P_{endo} and P_{exo} respectively at 0nN and 22.02 and 25.54 kcal/mol respectively at 4nN. A full geometry optimization at the CAM-B3LYP/6-311++G(2df,2p) at 0 nN gives 26.22 kcal/mol for P_{endo} and 28.08 kcal/mol for P_{exo} . The barrier values computed at the B3LYP/6-31G(d,p) level are lowered to 20.96 and 21.86 kcal/mol for the P_{endo} and P_{exo} adducts respectively at zero nN and to 20.02 and 26.26 at 2.7 nN. Computations of full COGEF path under tension with the CAM-B3LYP and the B3LYP functionals led to severe convergence issues because these functionals are not well-suited to describe the diradical species that appear for values of the forces close to the first bond rupture and beyond.

At zero force and at 4 nN, single point barriers values computed at the wb97xD/6-311++G(d,p) level are essentially the same as those computed at wb97XD/6-31G(d,p) for the P_{endo} and the P_{exo} adducts. These results are summarized in Table S1 below.

Table S1. Computed values of the activation barrier at 298K for several functionals and basis sets.

‘SP’ means a single point computation on the geometry optimized at the UwB97XD/6-31G(d,p) level.

0 nN	Barrier ($\Delta G^{\ddagger 0}$) kcal/mol		Rates (Eyring) s⁻¹	
Level	P_{endo}	P_{exo}	P_{endo}	P_{exo}
UwB97XD/6-31G(d,p).	28.26	30.76	1.19 10 ⁻⁸	1.75 10 ⁻¹⁰
UBH&HLYP/6-31G(d,p)	30.51	32.24	2.67 10 ⁻¹⁰	1.44 10 ⁻¹¹
CAMB3LYP/6-311++G(2df,2p)	26.22	28.08	3.73 10 ⁻⁷	1.62 10 ⁻⁸
UwB97XD/6-311++G(d,p) SP	27.86	30.25	2.34 10 ⁻⁸	4.15 10 ⁻¹⁰
UB3LYP/6-31G(d,p) SP	20.65	not converged	4.52 10 ⁻³	
UB3LYP/6-31G(d,p)	20.96	21.86	0.0027	0.0006

2.7 nN	Barrier ($\Delta G^{\ddagger 0}$) kcal/mol		Rates (Eyring) s⁻¹	
Level	P_{endo}	P_{exo}	P_{endo}	P_{exo}
UwB97XD/6-31G(d,p)	31.46	39.62	5.38 10 ⁻¹¹	5.61 10 ⁻¹⁷
UBHLYP/6-31G(d,p)	34.06	40.51	6.68 10 ⁻¹³	1.25 10 ⁻¹⁷
UB3LYP/6-31G(d,p) SP	25.39	32.57	1.51 10 ⁻⁶	8.26 10 ⁻¹²
UB3LYP/6-31G(d,p)	20.02	26.26	1.31 10 ⁻²	3.49 10 ⁻⁷

4.05 nN	Barrier ($\Delta G^{\ddagger 0}$) kcal/mol		Rates (Eyring) s⁻¹	
Level	P_{endo}	P_{exo}	P_{endo}	P_{exo}
UwB97XD/6-31G(d,p)	18.09	22.40	0.34	2.36 10 ⁻⁴
UwB97XD/6-311++G(d,p) SP	18.58	22.02	0.15	4.48 10 ⁻⁴
UBHLYP/6-31G(d,p)	22.03	25.55	4.40 10 ⁻⁴	1.16 10 ⁻⁶
UB3LYP/6-31G(d,p) SP	not converged	not converged		
UB3LYP/6-31G(d,p)	not converged	not converged		

The rates of the first bond rupture for P_{exo} and P_{endo} computed with the wB97XD functional at 298K are shown in figure S3.

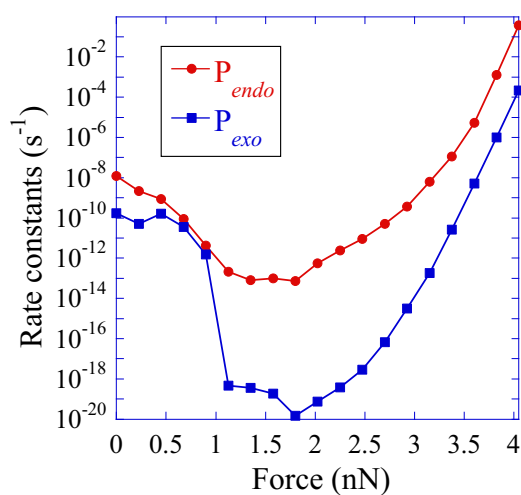


Figure S3: Computed rate constants at the UDFT/wB97XD level as a function of the pulling force up to the SB1 rupture for the two adducts. Files of the geometries of the reactant and transition states are given in the SI (S7).

S1.4 Diradicalar character of S_0 and T_0 and spin-orbit interaction

The CAS -SCF computations were carried out with an active space of 4 molecular orbitals and 4 active electrons (CAS(4,4)). S_0 has a diradical character in the intermediate region between the two bond ruptures. In that region, the two main configurations are that of the GS, $|2200\rangle$ and the HOMO-LUMO doubly excited configuration $|2020\rangle$. The CI coefficients are reported in Figure S4. In Figure S5, we report isocontours of the natural CAS orbitals. One can see that for distortions between 1.4 and 3.2 Å, the HOMO and the LUMO natural CAS MO's are delocalized on the two moieties. Since the coefficients on the $|2200\rangle$ and $|2020\rangle$ configurations are of opposite sign and roughly of the same magnitude, in the intermediate region, the S_0 wave function has a diradicalar character, see for example ref. ¹⁴.

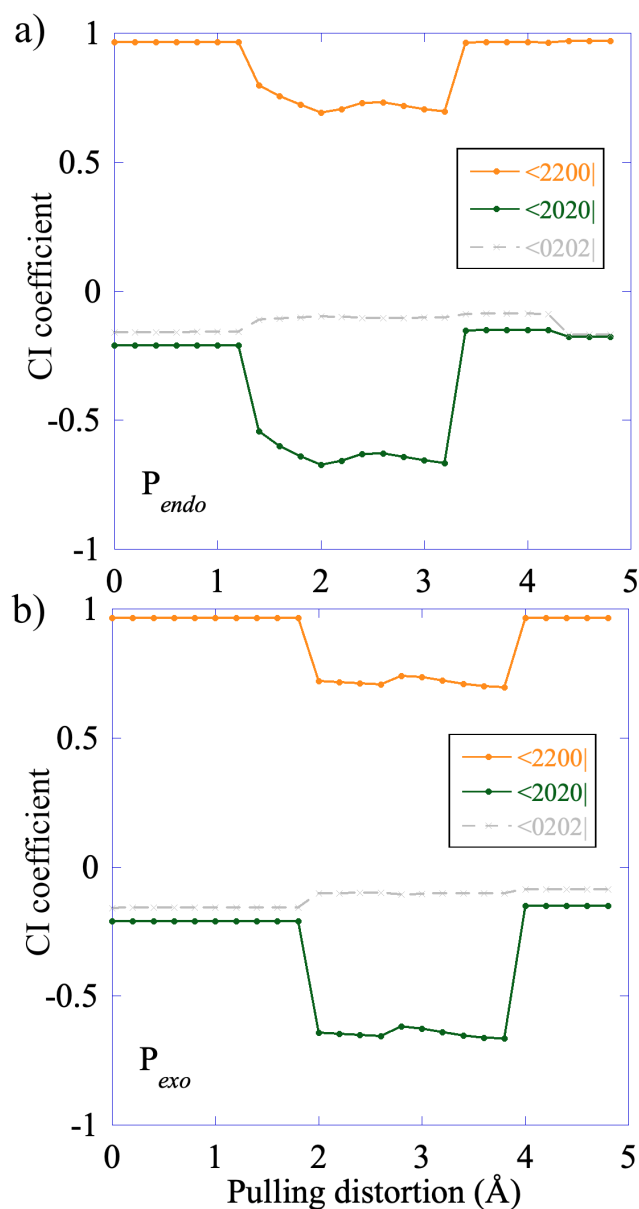
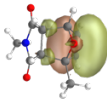
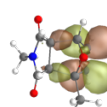
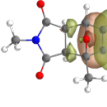
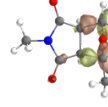


Figure S4. CI coefficients of the S_0 for the P_{endo} and the P_{exo} adducts. In the intermediate region, the coefficients of $|2200\rangle$ and $|2020\rangle$ are $\approx \sqrt{2}$ which leads to a diradical character since the natural HOMO and LUMO are delocalized over the two moieties, see Figure S5.

P_{endo}				P_{exo}			
CoGEF Point	Distortion [Å]	HOMO	LUMO	HOMO	LUMO	Distortion [Å]	CoGEF Point
0	0.0					0.0	0

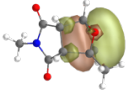
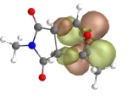
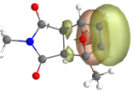
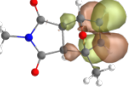
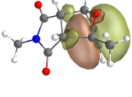
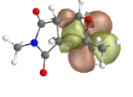
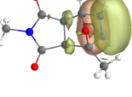
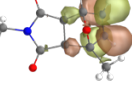
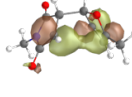
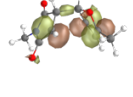
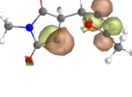
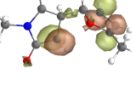
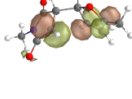
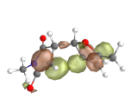
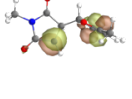
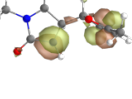
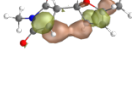
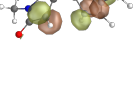
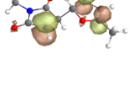
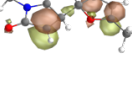
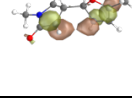
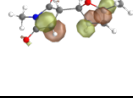
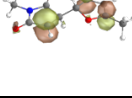
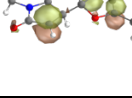
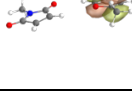
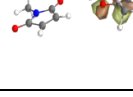
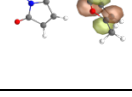
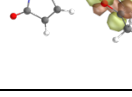
4	0.8					1.2	6
6	1.2					1.8	9
7	1.4					2.0	10
10	2.0					2.6	13
14	2.8					3.2	16
16	3.2					3.8	19
17	3.4					4.0	20

Figure S5. Isocontours of the natural CAS orbitals as a function of the pulling distortion along the CoGEF path for the P_{endo} and the P_{exo} adducts.

The energy of the lowest triplet state T_0 was computed along the CoGEF path at the geometries of the singlet S_0 . The main configuration is the $|2aa0\rangle$ configuration throughout the CoGEF path, with a weight larger than 93 % (Figure S6).

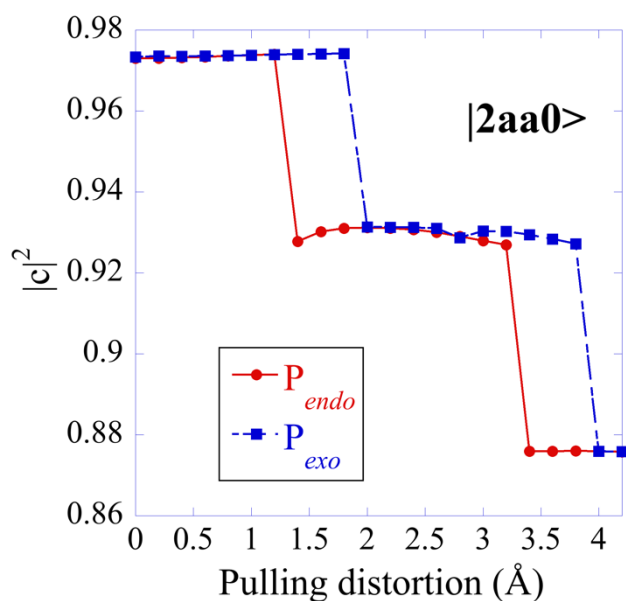


Figure S6: The weight of the $|2aa0\rangle$ configuration in the T_0 state determinantal composition along the CoGEF path.

We show in Figure S7 the S_0/T_0 energy difference along the CAS CoGEF path for the two adducts. The value of the spin-orbit coupling is reported in Table S1. The geometries of the minimum energy intersystem crossing (MEIC) for the P_{endo} and P_{exo} adducts are reported in Figure S8. One MEIC was identified for P_{endo} with a geometry close to the anti geometry along the minimum path. Two MEIC were localized for the P_{exo} adduct, one close to *anti* conformer and one close to *gauche* one.

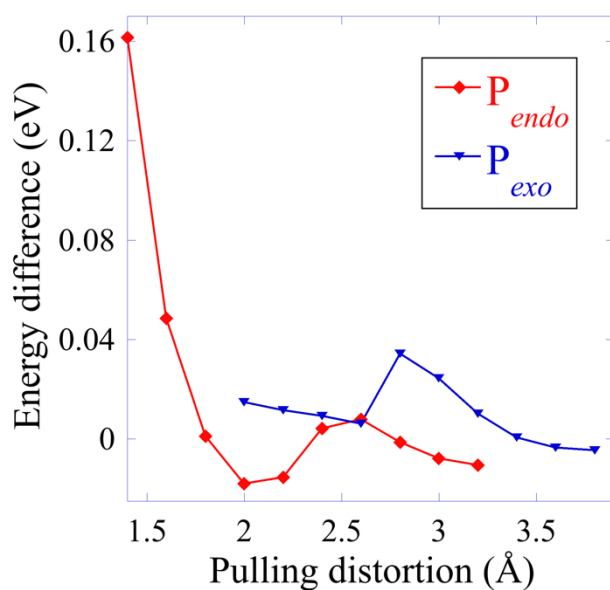


Figure S7: Energy differences T_0/S_0 computed at the CAS(4,4) level in the intermediate region.

Table S1: Spin-orbit coupling constants (cm^{-1}) computed at the geometries of the CoGEF pathway.

Distortion	P_{endo}	P_{exo}
0.0	0.733112	0.724825
0.20	0.717576	0.730484
0.40	0.699826	0.734509
0.60	0.683551	0.734170
0.80	0.669061	0.729655
1.0	0.655881	0.721678
1.2	0.644751	0.709301
1.4	0.121106	0.693892
1.6	0.067589	0.674935
1.8	0.031070	0.652809
2.0	0.002896	0.026728
2.2	0.026061	0.024470
2.4	0.046159	0.022635
2.6	0.047017	0.020343
2.8	0.034450	0.044373
3.0	0.023332	0.043400
3.2	0.014914	0.032134
3.4	0.033447	0.019743
3.6	0.079095	0.012212
3.8	0.080286	0.009061
4.0	0.087997	0.067316
4.2	0.099456	0.066679
4.4	0.116234	0.066630
4.6	0.118341	0.064166
4.8	0.116921	0.067069

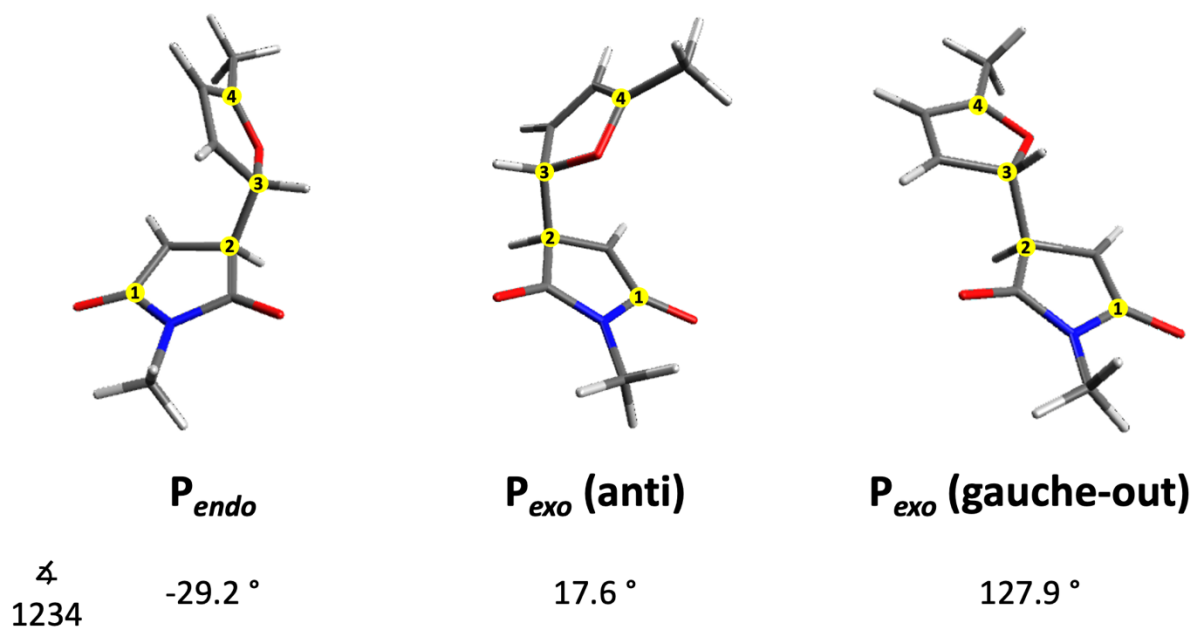


Figure S8: Geometries at the minimum energy intersystem crossings for P_{endo} and P_{exo} . The geometries are given in the SI (S8).

References

1. Beyer, M. K., The mechanical strength of a covalent bond calculated by density functional theory. *J. Chem. Phys.* 2000, 112, 7307-7312.
2. Chai, J.-D.; Head-Gordon, M., Long-range corrected hybrid density functionals with damped atom–atom dispersion corrections. *Phys. Chem. Chem. Phys.* 2008, 10, 6615-6620.
3. Knowles, P. J.; Werner, H.-J., An efficient second-order MC SCF method for long configuration expansions. *Chem. Phys. Lett.* 1985, 115, 259-267.
4. Brémond, E.; Adamo, C., Seeking for parameter-free double-hybrid functionals: The PBE0-DH model. *J. Chem. Phys.* 2011, 135, 024106.
5. Becke, A. D., A new mixing of Hartree–Fock and local density-functional theories. *J. Chem. Phys.* 1993, 98, 1372-1377.
6. Grimme, S.; Antony, J.; Ehrlich, S.; Krieg, H., A consistent and accurate ab initio parametrization of density functional dispersion correction (DFT-D) for the 94 elements H–Pu. *J. Chem. Phys.* 2010, 132, 154104.
7. Shao, Y., et al., Advances in molecular quantum chemistry contained in the Q-Chem 4 program package. *Mol. Phys.* 2015, 113, 184-215.
8. Werner, H.-J., et al., The Molpro quantum chemistry package. *J. Chem. Phys.* 2020, 152, 144107.
9. Werner, H.-J.; Knowles, P. J.; Knizia, G.; Manby, F. R.; Schütz, M., Molpro: a general-purpose quantum chemistry program package. *Wiley Interdiscip. Rev. Comput. Mol. Sci* 2012, 2, 242-253.
10. Wang, Z.; Craig, S. L., Stereochemical effects on the mechanochemical scission of furan–maleimide Diels–Alder adducts. *Chem. Comm.* 2019, 55, 12263-12266.

11. Meir, R.; Chen, H.; Lai, W.; Shaik, S., Oriented Electric Fields Accelerate Diels–Alder Reactions and Control the endo/exo Selectivity. *ChemPhysChem* 2010, 11, 301-310.
12. Yang, C., et al., Electric field–catalyzed single-molecule Diels-Alder reaction dynamics. *Sci. Adv.* 2021, 7, eabf0689.
13. Rulíšek, L.; Šebek, P.; Havlas, Z.; Hrabal, R.; Čapek, P.; Svatoš, A., An Experimental and Theoretical Study of Stereoselectivity of Furan–Maleic Anhydride and Furan–Maleimide Diels–Alder Reactions. *J. Org. Chem.* 2005, 70, 6295-6302.
14. Salem, L.; Rowland, C., The Electronic Properties of Diradicals. *Angew. Chem.* 1972, 11, 92-111.